

DETAILED CFD MODELLING OF FAST PYROLYSIS OF DIFFERENT BIOMASS TYPES IN FLUIDIZED BED REACTORS

Qitai Eri, Baolu Wang, Jing Peng, Xinjun Zhao and Ting Li *

School of Energy and Power Engineering, Beihang University, Beijing, China

In the present study, an Eulerian-Eulerian computational fluid dynamics (CFD) model, combined with a comprehensive biomass reaction scheme, was used to simulate fast pyrolysis of four different biomass types in the fluidized bed reactors. The study focuses on the influence of biomass components of different biomass types on the yields, formations, and contents of compositions of pyrolysis products. The result showed that the bio-oil yield of cellulose-rich biomass was higher than other biomass types, and char was mainly produced by the fast pyrolysis of LIG-C of biomass. Moreover, the contents of bio-oil components were affected by the fast pyrolysis of biomass components. Further, the energy recovery coefficient (ERC) of bio-oil obtained from pyrolysis of different biomass types was also calculated and analyzed in this paper.

Keywords: biomass, fast pyrolysis, fluidized bed reactor, CFD, energy recovery coefficient

INTRODUCTION

Currently, energy shortages and environmental pollution problems are very serious. The use of biomass to produce fuel is a way to solve these problems, because biomass is a renewable and clean energy source.^[1] There are various techniques to convert biomass into liquid fuels, among which fast pyrolysis can produce a liquid fuel effectively. Moreover, the fuel can be easily stored and transported.^[2] Thus, fast pyrolysis of biomass has been widely studied and used.

The use of computational fluid dynamics (CFD) coupled with a kinetic model to simulate fast pyrolysis of biomass is a convenient method.^[3] Much simulation work has been done to investigate fast pyrolysis of biomass. Papadis et al. modelled fast pyrolysis of wood to study heat, momentum, and mass transport in bubbling fluidized beds.^[4] Xue et al. investigated the pure cellulose and bagasse fast pyrolysis in fluidized bed reactors using a CFD model.^[5] The results showed that the pyrolysis of bagasse produces more char than cellulose pyrolysis.^[5] In another simulation work of Xue et al., they compared the product yields of five different biomass types to investigate the relationships between biomass components and product yields.^[6] Mellin et al. modelled biomass fast pyrolysis in different reaction atmospheres, and the composition of pyrolysis products were given and discussed in detail.^[3] Ranganathan and Gu simulated the fast pyrolysis of three different types of biomass, and the product yields were given and analyzed in their study.^[7]

Biomass is mainly composed of cellulose, hemicellulose, and lignin. The weight fraction of the three main compounds varies in different biomass types. It is reported that the char yield of lignin pyrolysis is higher than that of the pyrolysis of cellulose and hemicellulose.^[8] However, cellulose and hemicellulose contribute to the major portion of bio-oil during the biomass fast pyrolysis.^[8] Moreover, the compositional variations in biomass species have a great influence on the composition of products of pyrolysis.^[9] It was also found that the product properties resulting from different biomass types are significantly different.^[10] However, no simulation studies have been done on comparing the fast pyrolysis of different biomass types and analyzing the yields and composition of pyrolysis products in detail. Thus, it is important to investigate

the effects of different biomass types on product yields and the composition of products during the fast pyrolysis of biomass.

In the present study, CFD simulations were conducted for fast pyrolysis of bagasse, beech, oak, and pine in fluidized bed reactors and under the same operating conditions. For the simulation of multiphase flows, the Stokes numbers can be used as a guide for the selection of the simulation models, when $St > 1.0$, the Eulerian model is applicable.^[11] In our research, the Stokes number range of the biomass and sand phases are 5.51–23.03, so the Eulerian-Eulerian method was used in this work. This study aims to compare and analyze the fast pyrolysis of four different biomass types in detail. The yields of fast pyrolysis of different biomass types were compared, and the formation rate of char from different biomass components was analyzed. Then, the compositions of bio-oil obtained by fast pyrolysis of different biomass types were given, and the production of some bio-oil components was analyzed. Meanwhile, the formation rate and mass distribution of LVG (Levoglucosan) of bio-oil in the fluidized bed reactor was discussed. Furthermore, the ERCs of bio-oil were estimated and compared.

MODEL DESCRIPTION

A three-dimensional (3-D) fluidized bed reactor is modelled in the present study, and the geometry of the reactor is based on a 300 g/h fluidized bed reactor at Aston University, UK.^[12] The schematic of the fluidized bed reactor is shown in Figure 1. Sand was used as the heat transfer fluidizing medium in the fluidized bed reactor. The fluidization gas was preheated nitrogen (N_2), which flowed into the fluidized bed from the bottom of the reactor. Biomass was fed from the side of the reactor, and the gas products exited the fluidized bed reactor from the products outlet.

* Author to whom correspondence may be addressed.

E-mail address: li1329@buaa.edu.cn

Can. J. Chem. Eng. 96:2043–2052, 2018

© 2018 Canadian Society for Chemical Engineering

DOI 10.1002/cjce.23180

Published online 7 March 2018 in Wiley Online Library

(wileyonlinelibrary.com).

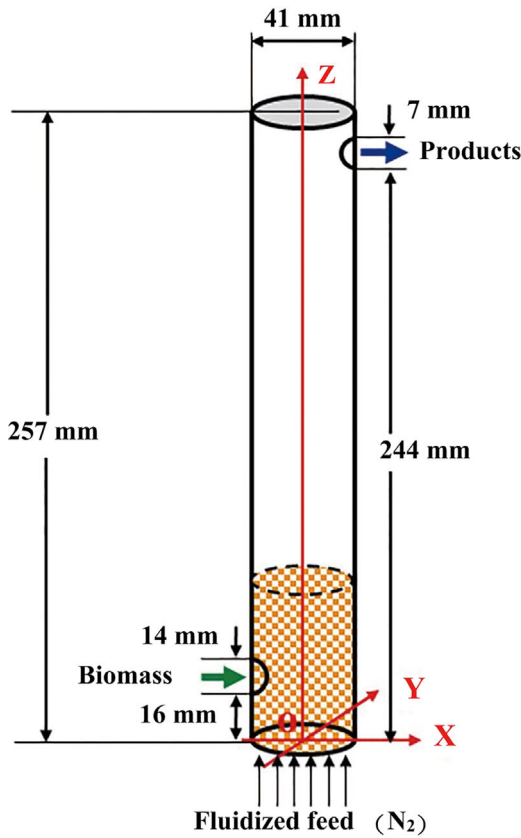


Figure 1. Schematic of the three-dimensional fluidized bed reactor.

COMPUTATIONAL MODEL

An Eulerian-Eulerian multiphase CFD model combined with a comprehensive kinetic model was used to investigate fast pyrolysis of different biomass types in fluidized bed reactors. The commercial software ANSYS Fluent 15.0 was used to conduct the numerical simulations.

Equations Governing Multiphase Flow

Three phases are considered in the fluidized bed reactor. They are the gas phase and two solid phases (biomass and sand). The gas phase is the primary phase, whereas biomass and sand are the secondary phases. All the phases are assumed to be interpenetrating continua in the Eulerian-Eulerian multiphase model.^[13]

Gas phase

The gas phase continuity can be represented as Equation (1):

$$\frac{\partial}{\partial t} (\alpha_g \rho_g) + \nabla \cdot (\alpha_g \rho_g \vec{v}_g) = \dot{m}_{bg} \quad (1)$$

where α is the volume fraction, v is the velocity, and \dot{m}_{bg} is the mass transfer from the biomass phase to gas phase (subscripts g and b denote gas and biomass, respectively).

The species transport in the gas phase is expressed as follows:

$$\frac{\partial}{\partial t} (\alpha_g \rho_g Y_i) + \nabla \cdot (\alpha_g \rho_g \vec{v}_g Y_i) = \dot{m}_{bgi} \quad (2)$$

where Y_i is the mass fraction of the i^{th} gas species and \dot{m}_{bgi} is the mass transfer from the biomass phase to gas phase component i .

The momentum conservation in the gas phase has the form:

$$\frac{\partial}{\partial t} (\alpha_g \rho_g \vec{v}_g) + \nabla \cdot (\alpha_g \rho_g \vec{v}_g \vec{v}_g) = -\alpha_g \nabla p + \alpha_g \rho_g \vec{g} + \nabla \cdot \bar{\tau}_g + K_{sg}(\vec{v}_g - \vec{v}_s) + K_{bg}(\vec{v}_b - \vec{v}_g) + \dot{m}_{bg} \vec{v}_b \quad (3)$$

where p is the pressure, \vec{g} is the gravitational force, and $\bar{\tau}_g$ is the gas phase stress-strain tensor. K_{sg} , and K_{bg} are interphase momentum exchange coefficients between the solid phase and gas phase (subscript s denotes sand). The gas-solid exchange coefficient is given by Gidaspow.^[14] The exchange coefficient K_{pg} (subscript p denotes the sand phase or biomass phase) can be represented as Equations (4)–(6).

$$K_{pg} = \frac{3}{4} C_D \frac{\alpha_p \alpha_g \rho_g |\vec{v}_p - \vec{v}_g|}{d_p} \alpha_g^{-2.65} \quad \text{when } \alpha_g > 0.8, \quad (4)$$

$$K_{pg} = 150 \frac{\alpha_p (1 - \alpha_g) \mu_g}{\alpha_g d_p^2} + 1.75 \frac{\rho_g \alpha_p |\vec{v}_p - \vec{v}_g|}{d_p} \quad \text{when } \alpha_g \leq 0.8, \quad (5)$$

$$C_D = \frac{24}{\alpha_g Re_p} \left[1 + 0.15 (\alpha_g Re_p)^{0.687} \right] \quad (6)$$

$$Re_p = \frac{\alpha_p \rho_g d_p |\vec{v}_p - \vec{v}_g|}{\mu_p} \quad (7)$$

where Re_p is the particle Reynolds number, and C_D is the drag coefficient.

The energy conservation of the gas phase is given by Equation (8).

$$\frac{\partial}{\partial t} (\alpha_g \rho_g h_g) + \nabla \cdot (\alpha_g \rho_g \vec{u}_g h_g) = \alpha_g \frac{\partial p}{\partial t} + \bar{\tau}_g : \nabla \vec{v}_g - \nabla \cdot \vec{q}_g + \nabla H_g + H_{gs} a_{gs} (T_g - T_s) + H_{gb} a_{gb} (T_g - T_b) \quad (8)$$

where h_g is the specific enthalpy of the gas phase, \vec{q}_g is the heat flux, and ΔH_g is the heat of the chemical reaction in the gas phase. The volumetric heat exchange coefficients (H_{gs} and H_{gb}) are given by Gunn:^[15]

$$H_{gp} = \frac{6k_g \alpha_g \alpha_p Nu_p}{d_p^2} \quad (9)$$

$$Nu_p = \left(7 - 10\alpha_g + 5\alpha_g^2 \right) \left(1 + 0.72 Re_p^{0.2} Pr^{1/3} \right) + \left(1.33 - 2.4\alpha_g + 1.2\alpha_g^2 \right) Re_p^{0.7} Pr^{1/3} \quad (10)$$

where k is the heat conductivity, Nu_p is the solids Nusselt number,^[14] which is approximated by following the work by Gunn,^[15] and Pr is the Prandtl number.

The gas phase stress-strain tensor $\bar{\tau}_g$ in Equation (3) and Equation (8) is defined as follows:

$$\bar{\tau}_g = \alpha_g \mu_g \left(\nabla \vec{v}_g + \nabla \vec{v}_g^T \right) + \alpha_g \left(\lambda_g - \frac{2}{3} \mu_g \right) \nabla \cdot \vec{v}_g \bar{I} \quad (11)$$

where μ_g is the shear viscosity of the gas phase, and λ_g is the bulk viscosity of the gas phase.

Solid phase

The continuity equation of the solid phase p is expressed as follows:

$$\frac{\partial}{\partial t}(\alpha_p \rho_p) + \nabla \cdot (\alpha_p \rho_p \vec{v}_p) = \dot{m}_{pg} \quad (12)$$

where \dot{m}_{pg} is the mass transfer from the solid phase p to the gas phase.

The momentum conservation for the solid phase p is given by Equation (13):

$$\begin{aligned} \frac{\partial}{\partial t}(\alpha_p \rho_p \vec{v}_p) + \nabla \cdot (\alpha_p \rho_p \vec{v}_p \vec{v}_p) = & -\alpha_g \nabla_p + \alpha_p \rho_p \vec{g} + \nabla \cdot \vec{\tau}_p \\ & + K_{np}(\vec{v}_n - \vec{v}_p) + K_{gp}(\vec{v}_g - \vec{v}_p) \end{aligned} \quad (13)$$

where K_{np} is the momentum exchange coefficient among n phases (n denotes the solid phase, excluding solid phase p) with solid phase p , and K_{gp} is the momentum exchange coefficient between the gas phase and solid phase p .

The energy conservation for solid phase p is given by Equation (14):

$$\begin{aligned} \frac{\partial}{\partial t}(\alpha_p \rho_p h_p) + \nabla \cdot (\alpha_p \rho_p \vec{u}_p h_p) = & \alpha_p \frac{\partial p_p}{\partial t} + \vec{\tau}_p \\ & : \nabla \vec{u}_p - \nabla \cdot \vec{q}_p + \nabla H_p + H_{pg} a_{pg} (T_p - T_g) \end{aligned} \quad (14)$$

where \vec{q}_p is the heat flux, ΔH_p is the heat of the reaction in the solid phase p . The solid phase stress-strain tensor $\vec{\tau}_p$ in Equations (13) and (14) can be represented as follows:

$$\vec{\tau}_p = -P_p \vec{I} + \alpha_p \mu_g (\nabla \vec{v}_p + \nabla \vec{v}_p^T) + \alpha_p \left(\lambda_p - \frac{2}{3} \mu_p \right) \nabla \cdot \vec{v}_p \quad (15)$$

where μ_p is the solid shear viscosity of the solid phase, and is defined as Equation (16). λ_p is the bulk viscosity of the solid phase, and can be represented as Equation (17). P_p denotes the solid phase pressure, and is defined as Equation (18):

$$\mu_p = \mu_{p,col} + \mu_{p,kin} + \mu_{p,fr} \quad (16)$$

where $\mu_{p,col}$ is the collisional viscosity, $\mu_{p,kin}$ is the kinetic viscosity, and $\mu_{p,fr}$ is the frictional viscosity.

$$\lambda_p = \frac{4}{3} \alpha_p \rho_p d_p g_{0,pp} (1 + e_{pp}) \left(\frac{\theta_p}{\pi} \right)^{1/2} \quad (17)$$

where e_{pp} denotes the coefficient of restitution for particle collisions. Here, as demonstrated in previous studies on gas-solid fluidized bed hydrodynamics, a restitution coefficients value of 0.9 provided more accurate simulation results,^[16–17] so 0.9 was selected as the coefficients of restitution for particles in this study. $g_{0,pp}$ is the radial distribution function, and θ_p is the granular temperature.

$$P_p = \alpha_p \rho_p \theta_p + 2 \rho_p (1 + e_{pp}) \alpha_p^2 g_{0,pp} \theta_p \quad (18)$$

The granular temperature of the solid phase p is proportional to the kinetic energy of the particles' random motion, and is given by Equation (19).

$$\theta_p = \frac{1}{3} u_{p,j} u_{p,j} \quad (19)$$

where $u_{p,j}$ is the j^{th} component of the fluctuating solids velocity.

The transport equation derived from the kinetic theory is defined as follows:

$$\begin{aligned} \frac{3}{2} \left[\frac{\partial}{\partial t}(\alpha_p \rho_p \theta_p) + \nabla \cdot (\alpha_p \rho_p \vec{v}_p \theta_p) \right] = & -(P_p \vec{I} + \vec{\tau}_p) \\ & : \nabla \vec{v}_p + \nabla \cdot (\sigma_{\theta_p} \nabla \theta_p) - \gamma_{\theta_p} + \varphi_{N\theta_p} \end{aligned} \quad (20)$$

where σ_{θ_p} is the diffusion coefficient, σ_{θ_p} is the collisional dissipation of energy, and $\varphi_{N\theta_p}$ is the energy exchange between the n^{th} gas or solid phase and the solid phase p . Particle flows in the reactor were described using a kinetic theory of granular flow. Granular bulk viscosity for the sand is calculated according to Lun et al.,^[18] and granular viscosity is calculated according to Syamlal.^[19]

Biomass Pyrolysis Model

The reaction kinetics scheme of biomass fast pyrolysis (Reactions 1–25) is shown in Table 1. The same kinetics scheme has also been used in the authors' previous work.^[20] The scheme is developed by Ranzi et al.,^[21] and is an extension of the previous work of Ranzi et al.^[22] The extension reaction kinetics scheme is based on the multi-step devolatilization and decomposition of biomass. Moreover, the scheme of biomass pyrolysis is modified taking advantage of the recent literature and comparing the reaction kinetics scheme predictions with experimental data. Thus, the kinetics scheme can provide more detailed information on biomass pyrolysis. The drying reaction (Reaction 26) used in the simulation was obtained from other literature.^[23]

All reactions are modelled according to the first-order Arrhenius law, given by Equation (21):

$$k = A e^{-E/RT} \quad (21)$$

where k is the reaction rate constant, A is the pre-exponential factor, and E is the activation energy. The temperature, concentration gradient, and diffusion inside the particle are neglected in the numerical simulation.

Solution Methodology

The boundary conditions used in this simulation work were based on the experimental conditions used in the work of Patel.^[12] 150 g sand was used in the fluidized bed, and the sand volume fraction was about 0.618. The mass flow rate of the biomass was 213.41 g/h, whereas the inlet velocity of the preheated N_2 was 0.744 m/s. The temperature of the feeding biomass was 300 K, while the temperature of the preheated N_2 was 773 K. The atmospheric pressure outlet condition was used at the product outlet, while the no-slip and adiabatic wall conditions were used for all the walls of the fluidized bed reactor. The physical properties of sand, char, and different biomass types are obtained from different literature.^[12,24–28] The boundary condition used in the present simulations is given in Table 2, while the physical properties of solid particles are given in Table 3.

Table 1. Reaction kinetics scheme of biomass pyrolysis^[21,23]

	Reactions	Kinetic constants (1/s)*
R1	CELL → CELLA	$4 \times 10^{13} \exp(-45000/RT)$
R2	CELLA → 0.8HAA + 0.2GLYOX + 0.1CH ₃ HCO + 0.25HMFU + 0.3C ₃ H ₆ O + 0.21CO ₂ + 0.1H ₂ + 0.4CH ₂ O + 0.16CO + 0.83H ₂ O + 0.02HCOOH + 0.61Char	$5 \times 10^8 \exp(-29000/RT)$
R3	CELLA → LVG	$1.8 \text{Texp}(-10000/RT)$
R4	CELL → 6Char + 5H ₂ O	$4 \times 10^7 \exp(-31000/RT)$
R5	HCE → 0.4HCE1 + 0.6HCE2	$3.3 \times 10^9 \exp(-31000/RT)$
R6	HCE1 → 0.025H ₂ O + 0.5CO ₂ + 0.025HCOOH + 0.5CO + 0.8CH ₂ O + 0.125C ₂ H ₅ OH + 0.1CH ₃ OH + 0.25C ₂ H ₄ + 0.125G{H ₂ } + 0.275G{CO ₂ } + 0.4G{COH ₂ } + 0.45G{CH ₃ OH} + 0.325G{CH ₄ } + 0.875Char	$1 \times 10^9 \exp(-32000/RT)$
R7	HCE1 → 0.25H ₂ O + 0.5CO ₂ + 0.05HCOOH + 0.3CO + 0.15G{CO} + 0.25G{CO ₂ } + 1.7G{COH ₂ } + 0.625G{CH ₄ } + 0.375G{C ₂ H ₄ } + 0.675 Char	$0.05 \text{Texp}(-8000/RT)$
R8	HCE1 → XYLAN	$0.9 \text{Texp}(-11000/RT)$
R9	HCE2 → 0.2H ₂ O + 0.175CO + 0.275CO ₂ + 0.5CH ₂ O + 0.1C ₂ H ₅ OH + 0.2HAA + 0.025HCOOH + 0.25G{CH ₄ } + 0.3G{CH ₃ OH} + 0.275G{C ₂ H ₄ } + 0.4G{CO ₂ } + 0.925G{COH ₂ } + Char	$3.3 \times 10^9 \exp(-33000/RT)$
R10	LIGC → 0.35LIGCC + 0.1COUMARYL + 0.08PHENOL + 0.41C ₂ H ₄ + H ₂ O + 0.3CH ₂ O + 0.32CO + 0.7G{COH ₂ } + 0.495 G{CH ₄ } + 5.735Char	$1.33 \times 10^{15} \exp(-48500/RT)$
R11	LIGH → LIGOH + C ₃ H ₆ O	$6.7 \times 10^{12} \exp(-37500/RT)$
R12	LIGO → LIGOH + G{CO ₂ }	$3.3 \times 10^8 \exp(-25500/RT)$
R13	LIGCC → 0.3COUMARYL + 0.2PHENOL + 0.35HAA + 0.7H ₂ O + 0.4CO + 0.65G{CH ₄ } + 0.6G{C ₂ H ₄ } + G{COH ₂ } + 0.4G{CO} + 6.75Char	$1.6 \times 10^6 \exp(-31500/RT)$
R14	LIGOH → LIG + 0.15G{H ₂ } + 0.9H ₂ O + 0.1CH ₄ + 0.5CH ₃ OH + 0.5G{CH ₃ OH} + 0.05CO ₂ + 0.3CO + G{CO} + 0.05HCOOH + 0.6G{COH ₂ } + 0.35G{CH ₄ } + 0.2G{C ₂ H ₄ } + 4.15Char	$5 \times 10^7 \exp(-30000/RT)$
R15	LIGOH → 1.5H ₂ O + 0.5CO + 0.1CH ₄ + 0.5G{H ₂ } + 1.6G{CO} + 3.9G{COH ₂ } + 1.65G{CH ₄ } + 0.3 G{C ₂ H ₄ } + 0.5G{CH ₃ OH} + 10.15Char	$33 \exp(-15000/RT)$
R16	LIG → FE2MACR	$2.4 \text{Texp}(-12000/RT)$
R17	LIG → 0.95H ₂ O + 0.2CH ₂ O + 0.4CH ₃ OH + CO + 0.2CH ₄ + 0.05HCOOH + 0.45G{CO} + 0.5G{COH ₂ } + 0.4G{CH ₄ } + 0.65G{C ₂ H ₄ } + 0.2C ₂ H ₄ O + 0.2C ₃ H ₆ O + 5.5Char	$4 \times 10^8 \exp(-30000/RT)$
R18	LIG → 0.6H ₂ O + 0.4CO + 0.2CH ₄ + 0.4CH ₂ O + 0.2G{CO} + 0.4G{CH ₄ } + 0.5G{C ₂ H ₄ } + 0.4G{CH ₃ OH} + 2G{COH ₂ } + 6Char	$0.083 \text{Texp}(-8000/RT)$
R19	G{CO ₂ } → CO ₂	$1 \times 10^6 \exp(-24000/RT)$
R20	G{CO} → CO	$5 \times 10^{12} \exp(-50000/RT)$
R21	G{COH ₂ } → CO + H ₂	$5 \times 10^{11} \exp(-71000/RT)$
R22	G{H ₂ } → H ₂	$5 \times 10^{11} \exp(-75000/RT)$
R23	G{CH ₄ } → CH ₄	$5 \times 10^{12} \exp(-71700/RT)$
R24	G{C ₂ H ₄ } → C ₂ H ₄	$5 \times 10^{12} \exp(-71700/RT)$
R25	G{CH ₃ OH} → CH ₃ OH	$2 \times 10^{12} \exp(-50000/RT)$
R26	H ₂ O(l) → H ₂ O(g)	$5.3 \times 10^{10} \exp(-21000/RT)$

* Activation energy expressed in kcal/kmol

The mesh used in the model consists of 19 780 hexagonal cells, has 90 nodes in the Z-direction, and has a grid side length size of 2.6–3.5 mm. In the X and Y-direction, grid size varies as the mesh conforms to the cylindrical shape. However, the cells are 2.56 mm in average in both the X and Y-direction. The grid used for simulation is shown in Figure 2. When performing the calculations, the time step of simulation was 0.0001 s. Momentum equations were resolved with a second order accurate upwind scheme. The QUICK scheme was used to solve the volume fraction equations. The governing equations were solved using the phase-coupled SIMPLE algorithm. The effect of turbulence was modelled using the k-ε turbulence model, which was proposed by Launder and Spalding.^[29] The *k* represents the turbulence kinetic energy, and the ε represents the dissipation rate. The turbulence kinetic energy, *k*, and its rate of dissipation, ε, are obtained from the following transport equations:

$$\frac{\partial}{\partial t}(\rho k) + \frac{\partial}{\partial x_i}(\rho k u_i) = \frac{\partial}{\partial x_j} \left[\left(\mu + \frac{\mu_t}{\sigma_k} \right) \frac{\partial k}{\partial x_j} \right] + G_k + G_b - \rho \varepsilon - Y_M + S_k \quad (22)$$

Table 2. Boundary conditions used in this study

Biomass inlet	
Mass flow (kg/s)	5.93×10^{-5}
Temperature (K)	300
Fluidizing gas inlet	
Velocity (m/s)	0.744
Temperature (K)	773
Walls	
Heat flux (W/m ²)	0
Momentum shear condition	No slip condition
Outlet	
Pressure (Pa)	101 325

Table 3. Physical properties of particle phases^[11,21–24]

	Diameter (mm)	Density (kg/m ³)	Specific heat capacity (J/kg · K)
Sand	0.55	2650	835
Char	–	350	1583
Bagasse	0.625	1757.44	1125
Beech	0.625	680	1500
Oak	0.625	660	1300
Pine	0.625	490	1150

and

$$\frac{\partial}{\partial t}(\rho \varepsilon) + \frac{\partial}{\partial x_i}(\rho \varepsilon u_i) = \frac{\partial}{\partial x_j} \left[\left(\mu + \frac{\mu_t}{\sigma_\varepsilon} \right) \frac{\partial \varepsilon}{\partial x_j} \right] + C_{1\varepsilon} \frac{\varepsilon}{k} (G_k + C_{3\varepsilon} G_b) - C_{2\varepsilon} \rho \frac{\varepsilon^2}{k} + S_\varepsilon \quad (23)$$

In these equations, G_k represents the generation of turbulence kinetic energy due to the mean velocity gradients. G_b is the generation of turbulence kinetic energy due to buoyancy. Y_M represents the contribution of the fluctuating dilatation in compressible turbulence to the overall dissipation rate. $C_{1\varepsilon}$, $C_{2\varepsilon}$, and $C_{3\varepsilon}$ are constants. σ_k and σ_ε are the turbulent Prandtl numbers for k and ε , respectively. S_k and S_ε are user-defined source terms.

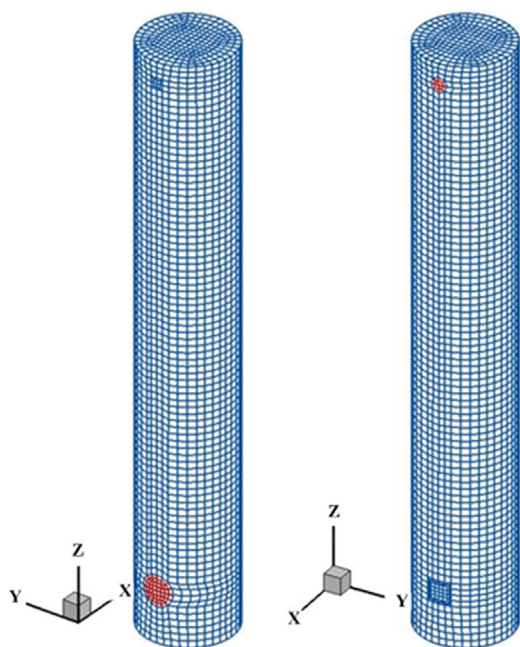
The turbulent viscosity, μ_t , is computed by combining k and ε as follows:

$$\mu_t = \rho C_\mu \frac{k^2}{\varepsilon} \quad (24)$$

where C_μ is a constant.

The model constants $C_{1\varepsilon}$, $C_{2\varepsilon}$, C_μ , σ_k , and σ_ε have the following default values:

$$C_{1\varepsilon} = 1.44, C_{2\varepsilon} = 1.92, C_\mu = 0.09, \sigma_k = 1.0, \sigma_\varepsilon = 1.3$$

**Figure 2.** Computational grids of the fluidized bed reactor.

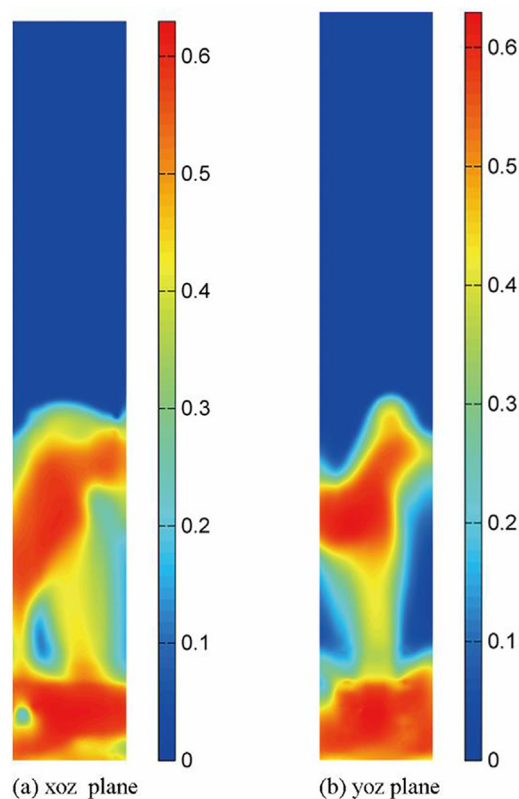
These default values have been determined from experiments for fundamental turbulent flows including frequently encountered shear flows like boundary layers, mixing layers, and jets, as well as for decaying isotropic grid turbulence. They have been found to work fairly well for a wide range of wall-bounded and free shear flows.

The stiff heterogeneous chemistry in ANSYS Fluent 15.0 was used to conduct the simulation of the heterogeneous reactions of biomass pyrolysis. The simulations were conducted for a real reaction time of around 30 s. During the simulation, the data files were saved regularly. The yields of biomass pyrolysis products were obtained by taking the average results of the last 5 s of the simulations.

RESULTS AND DISCUSSION

Hydrodynamic Study

A hydrodynamic study was carried out in the fluidized bed reactor. Sand is an important medium, as it could help the mixing and heat transfer in the fluidized bed reactor. Figure 3 shows snapshots of the sand volume fraction in two vertical planes in the fluidized bed

**Figure 3.** Snapshots of sand volume fractions of oak fast pyrolysis.

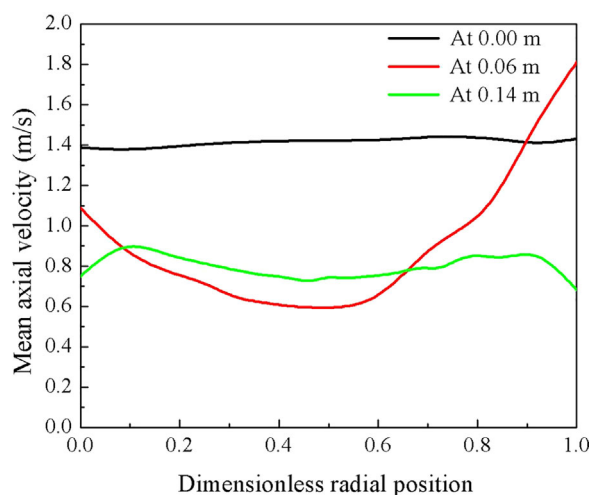


Figure 4. Mean axial velocity of gas at various locations in xoz plane of bagasse fast pyrolysis.

reactor. The bubbles in the fluidized bed reactor indicated that the sand was in good fluidizing condition. Figure 4 shows the mean axial velocity of gas at three different locations along the reaction height in the fluidized bed reactor. As can be seen in Figure 4, the mean axial velocity of gas at the fluidizing gas inlet ($z = 0.00$ m) was about 1.4 m/s, which is much higher than the velocity of fluidizing gas set in the fluidizing gas inlet (0.744 m/s). The reason for this phenomenon is that the sand in the fluidized bed reactor reduced the flow area of gas; thus, the gas accelerates at the fluidizing gas inlet. The velocity profile at 0.06 m shows that the velocity at the centre of the reactor is lower, and near the wall the velocity is higher. This is because that the velocity of gas is influenced by the fluidization of sand. Sand particles at the centre of the fluidized bed reactor try to come down, and negative velocity was observed in the centre of the reactor.^[7] Therefore, under the effect of sand the velocity of gas decreased in the centre of the fluidized bed reactor at 0.06 m. The velocity profile at 0.06 m also shows that the velocity near the left side of the wall was lower than that near the right side of the wall. This is because the biomass feedstocks were fed in the fluidized bed reactor from the left side (see Figure 1), and the biomass particles influenced the flow of gas. The velocity profile of gas at 0.14 m became uniform, because the location ($z = 0.14$ m) was above the fluidized sand bed and the gas velocity was not affected by sand. The gas velocity near the wall at 0.14 m was low, because the restriction near the wall is more in the form of shear stress.

Comparison of the Distribution of Products

The compositions of different biomass types are given in Table 4. As shown in Table 4, biomass consists of three major components, namely cellulose, hemicellulose, and lignin. Lignin can be divided into three different components, which are LIG-C, LIG-H, and

Table 5. Comparison of the experimental data and simulation results of bagasse fast pyrolysis

	Experimental data	Simulation Results	Relative Error (%)
Organic liquid (yield % db)	63.38	66.28	4.57
Total liquid (yield %)	75.00	74.51	-0.65

* The total liquid minus the total water is the total organic liquid

*Relative error = $\frac{\text{simulation result} - \text{experimental result}}{\text{experimental result}} \times 100\%$

LIG-O. LIG-C is representative of a softwood lignin and is richer in carbon, while LIG-H and LIG-O are representative of the structures of hardwood lignin and are richest in hydrogen and oxygen, respectively.^[29] The moisture and ash contents of bagasse can be found in the work of Patel.^[12] Firstly, the simulation of fast pyrolysis of bagasse was conducted, and the simulation results were compared with the experimental values from the work of Patel.^[12] As shown in Table 5 the relative errors between the simulation results and the reported experimental pyrolysis yields were found within 5 %. Thus, the model showed a very promising ability to investigate the fast pyrolysis of different biomass types.

It is well known that the biomass composition has a great influence on the yields of pyrolysis products. As shown in Figure 5, the yields of bio-oil obtained from pyrolysis of these four biomass types were over 70 %. The bio-oil yield of fast pyrolysis of oak is the highest (~77 %), while the bio-oil yield of fast pyrolysis of bagasse was the lowest (~71 %). Meanwhile, as shown in Table 4, the cellulose content of oak is the highest among the four biomass types, while that of bagasse is the lowest. The simulation result was in accordance with the results of other studies,^[5,6] which found that the cellulose-rich biomass tends to produce more bio-oil than other biomass. As shown in Figure 5, the gas yield obtained from the bagasse pyrolysis was the highest, while the gas yields obtained from the fast pyrolysis of other biomass types were almost the same. The yield of char produced by the fast pyrolysis of oak was the lowest, while the char yields obtained from the fast pyrolysis of other biomass types were almost the same (~11 %). According to previous studies, the lignin-rich material would like to produce more char.^[30–32] However, the simulation result of char yield versus the total lignin content of each biomass type was not always consistent with that finding (see Table 4 and Figure 5). Thus, the formation rate of char in the fluidized bed reactors was analyzed. Figure 6 shows the instantaneous formation rate of char as produced by four different biomass types. As shown in Figure 6, it is obvious that lignin contributes more to the formation of char than cellulose and hemicellulose. However, different components of lignin make different contributions to the formation rate of char. Bagasse only contains LIG-C, so only LIG-C contributes to the formation of char during the fast pyrolysis of the lignin of

Table 4. Compositions of different biomass types

Feedstock	weight percentage (%) of dry feed basis (db)						Reference
	Cellulose	Hemicellulose	Lignin	LIG-C	LIG-H	LIG-O	
Bagasse	36	47	17	17	0	0	Blondeau and Jeanmart ^[23]
Beech	48	28	24	11	0	13	Blondeau and Jeanmart ^[23]
Oak	51	27.80	21.2	3.20	2.90	15.10	Authiera et al. ^[30]
Pine	45	28	27	7	10	10	Anca-Couce et al. ^[26]

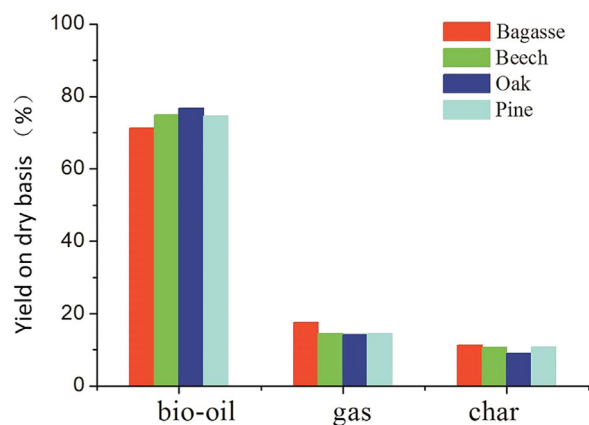


Figure 5. Distribution of the pyrolysis products of different biomass types.

bagasse. As shown in Figure 6b, LIG-C contributes more to the formation of char than LIG-O, though beech contains more LIG-O than LIG-C. The contents of LIG-C and LIG-H in oak are almost the same, but LIG-C shows a stronger ability to produce char than LIG-H (see Figure 6c). The same result could also be found in Figure 6d. Thus, it is clear that LIG-C contributes more to the formation of char than LIG-H and LIG-O. The simulation result was in accordance with the previous experimental study.^[33] Jakab et al.^[33] compared thermal decomposition of four kinds of softwood lignins and eleven kinds of hardwood lignins, and found that softwood lignins would produce more char than hardwood lignins.

Comparison of Bio-Oil Components

Bio-oil is a complex mixture that contains a variety of components. The physical and chemical properties of each component of the bio-oil influence the properties of bio-oil. Thus, studying the content of each component of bio-oil is the basis of investigating the various properties of bio-oil. Furthermore, it is also useful to obtain certain components of bio-oil.

Table 6 shows the contents of each composition of bio-oil obtained from pyrolysis of four different biomass types. The content of each component varied among different bio-oil types. As shown in Table 6, LVG, HAA, xylan, formaldehyde, HMFU, and water are the main components of bio-oil. It is obvious that the contents of LVG in bio-oil obtained from fast pyrolysis of these four biomass types were the highest (> 35 %). Furthermore, the weight fraction of LVG in the bio-oil obtained by the fast pyrolysis of oak was the highest, and is nearly 40 %. As shown in Table 1, LVG was obtained from the pyrolysis of cellulose. The cellulose content of oak was the highest among these four biomass types (see Table 4); thus, the LVG content of the bio-oil produced by fast pyrolysis of oak was the highest (see Table 6).

The formation of LVG in a fluidized bed reactor was analyzed in this paper. As shown in Figure 7a, the temperature of biomass at the biomass inlet of the fluidized bed reactor was low. As the biomass entered the fluidized bed reactor and mixed with the sand, the temperature of the biomass increased rapidly. The biomass temperature distribution in the fluidized bed reactor was more uniform than that at the biomass inlet. As shown in Figure 7b, the mass distribution of cellulose in the region where the biomass temperature was low (see Figure 7a) was higher than

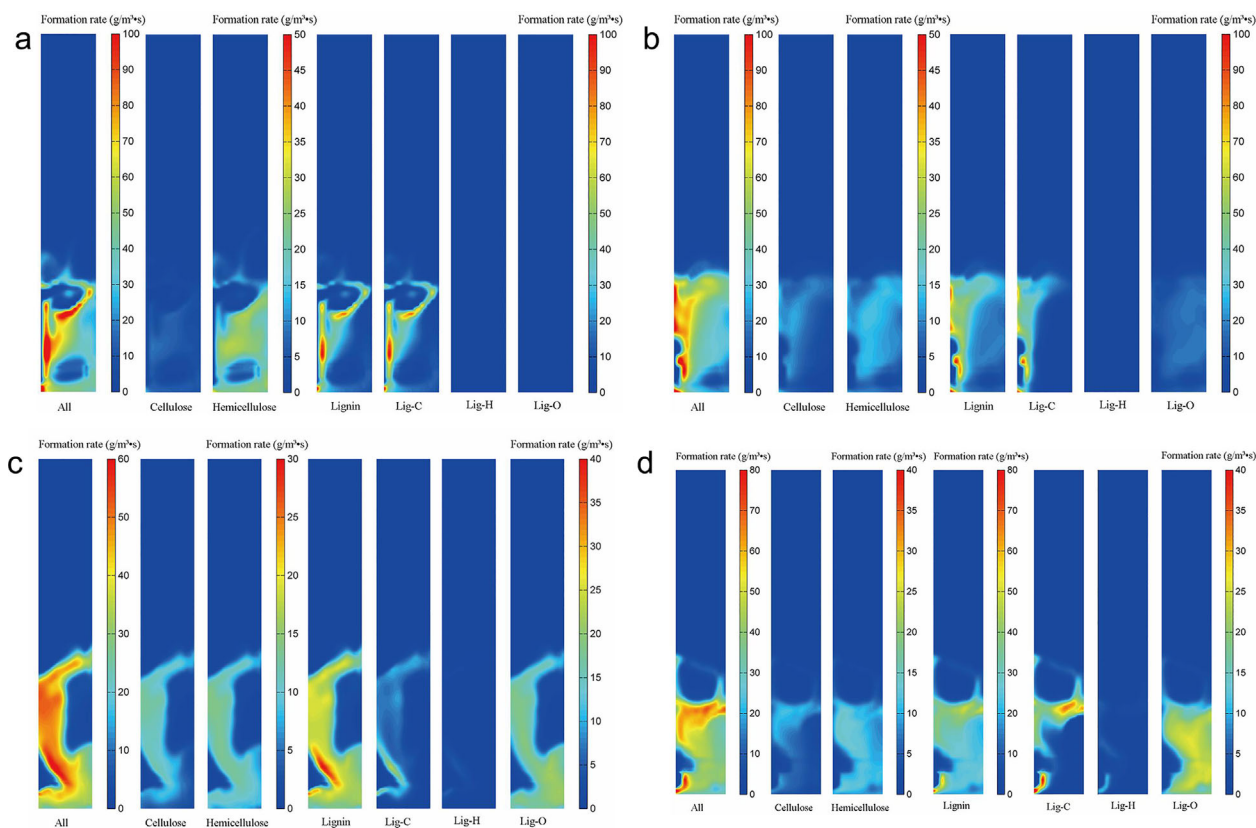


Figure 6. Instantaneous formation rate of char as produced by the fast pyrolysis of different biomass types and their biomass components: (a) bagasse and different biomass components of bagasse, (b) beech and different biomass components of beech, (c) oak and different biomass components of oak, (d) pine and different biomass components of pine.

Table 6. Composition of bio-oil from pyrolysis of different biomass types

Species	Formula	weight percentage (%) of bio-oil			
		Bagasse	Beech	Oak	Pine
Xylan	C ₅ H ₈ O ₄	15.43	7.74	7.3	7.48
Levogluconan (LVG)	C ₆ H ₁₀ O ₅	35.02	39.12	40	35.65
Hydroxymethylfurfural (HMFU)	C ₆ H ₆ O ₃	5.50	7.40	7.	7.29
Formaldehyde	CH ₂ O	11.48	8.11	7.4	8.00
Hydroxyacetaldehyde (HAA)	C ₂ H ₄ O ₂	13.40	13.80	13.5	13.60
Ethanol	C ₂ H ₅ OH	2.43	1.28	1.19	1.29
Phenol	C ₆ H ₅ OH	0.85	0.53	0.15	0.34
Acetaldehyde	CH ₃ HCO	0.77	1.18	1.2	1.26
Methanol	CH ₃ OH	0.58	1.39	1.7	2.04
Glyoxal	C ₂ H ₂ O ₂	2.02	2.73	2.7	2.68
Coumaryl	C ₉ H ₁₀ O ₂	1.71	1.06	0.3	0.69
Formic-acid	HCOOH	0.86	0.71	0.7	0.79
FE2MACR	C ₁₁ H ₁₂ O ₄	0.00	3.35	4.	5.06
Acetone	C ₃ H ₆ O	3.04	4.29	4.9	6.52
Water	H ₂ O	6.91	7.29	6.	7.33

other regions. The reason is that the pyrolysis of cellulose tended to react in a high temperature region to produce pyrolysis products. This was in accordance with the result shown in Figure 7c that the formation rate of LVG in the high temperature region of biomass was higher than other regions in the fluidized bed reactor. Figure 7d shows the mass distribution of LVG in the fluidized bed reactor. As can be seen from the figure, the mass distribution of LVG was higher in the region where the LVG formation rate was high. Moreover, under the drive of fluidization gas, LVG flowed to the outlet of the product.

Table 7 analyzes the source of formaldehyde and HAA in biomass. As can be seen from the table, most of the formaldehyde (> 55 %) was obtained from the fast pyrolysis of hemicellulose of biomass. Some of the formaldehyde was obtained from cellulose pyrolysis, while only a small amount was derived from lignin pyrolysis. It is obvious that about 73 % of formaldehyde in the bio-oil obtained from bagasse pyrolysis was from hemicellulose pyrolysis. The reason is that the hemicellulose content of bagasse was higher than the hemicellulose contents of other biomass

types. Thus, as shown in Table 6, the weight fraction of formaldehyde in bio-oil obtained from fast pyrolysis of bagasse was the highest. As can be seen from Table 7, cellulose contributed the most HAA production, while fast pyrolysis of lignin just contributed a small amount to the production of HAA. As shown in Table 4, the cellulose content of bagasse is the lowest among these four biomass types, while the hemicellulose content of bagasse was the highest. Thus, the weight percentage of HAA obtained from the hemicellulose fast pyrolysis of bagasse was the highest, while that obtained from the cellulose fast pyrolysis of bagasse was the lowest.

Bio-Oil HHV and ERC Analysis

The main product of biomass fast pyrolysis is bio-oil. Bio-oil is a high energy renewable fuel. Therefore, it is necessary to analyze the energy content of bio-oil and estimate the energy conversion efficiency of the fast pyrolysis of biomass. Thus, in the present study, the energy recovery coefficient (ERC) of bio-oil was introduced and defined as follows:

$$ERC_{\text{bio-oil}} = \frac{HHV_{\text{bio-oil,dry}} \times m_{\text{bio-oil,dry}}}{HHV_{\text{biomass,dry}} \times m_{\text{biomass,dry}}} \times 100 \% \quad (25)$$

where HHV is the high heating value, m is the mass, subscript 'bio-oil, dry' denotes the dry weight of bio-oil, and subscript 'biomass, dry' denotes the dry weight of biomass. The equation used to predict the HHV of biomass was developed by Yin,^[34] and is given by Equation (26).

$$HHV = 0.2949C + 0.8250H \text{ (MJ/kg)} \quad (26)$$

where, C and H represent the carbon and hydrogen contents of biomass, respectively. The equation has a mean absolute error lower than 5 % and marginal mean bias error at just 0.57 %.^[34]

The equation used to calculate the HHV of bio-oil was developed by Channiwalla and Parikh,^[35] and is given by Equation (27):

$$HHV = 0.3491C + 1.1783H + 0.1005S - 0.1034O - 0.0151N - 0.0211A \text{ (MJ/kg)} \quad (27)$$

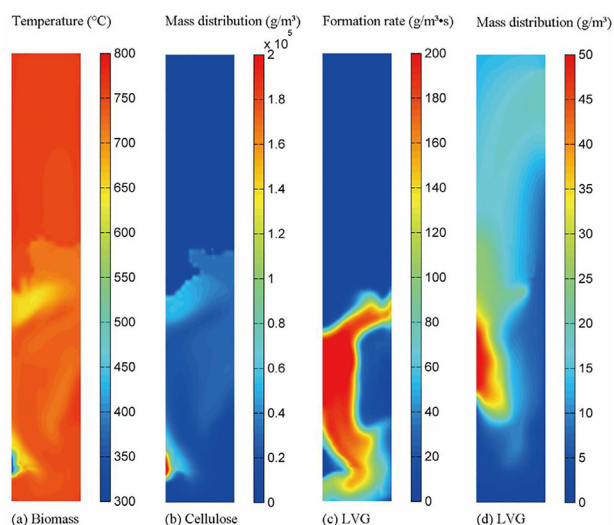


Figure 7. Instantaneous contours of temperature of biomass (oak), mass distribution of cell, formation rate of LVG, and mass distribution of LVG in the fluidized bed reactor.

Table 7. Source analysis of formaldehyde and HAA produced by fast pyrolysis of different biomass types

	weight percentage (%) of Formaldehyde				weight percentage (%) of HAA			
	Bagasse	Beech	Oak	Pine	Bagasse	Beech	Oak	Pine
Cellulose	18.24	34.76	37.92	34.67	62.51	81.74	82.71	81.65
Hemicellulose	72.98	55.04	56.39	56.37	37.40	18.18	17.23	18.29
Lignin	8.78	10.20	5.69	8.95	0.09	0.08	0.06	0.06

where, C, H, O, N, S, and A represent the carbon, hydrogen, oxygen, nitrogen, sulphur, and ash contents of bio-oil, respectively. Moreover, it is reported that the equation has an average absolute error of 1.45 %.^[35]

As given in Equations (26) and (27), the HHV of biomass and bio-oil depends on the contents of chemical elements. The HHV of materials has a close relationship with the O/C value, and a high O/C value probably gives a relatively low HHV of materials.^[31] As shown in Table 8, the O/C value of oak was the highest; thus, the HHV of oak was the lowest. Whereas the O/C values of the other three biomass types were almost the same and lower than that of oak. The HHV values of bagasse, beech, and pine were almost the same and higher than that of oak. Moreover, the same trend could be found in the relationship of the O/C value of bio-oil versus the HHV of the bio-oil. As shown in Equation (25), the energy recovery coefficient of bio-oil is related to the HHV of biomass and bio-oil, and the yield of bio-oil. The results in Table 8 show that the energy recovery coefficient of bio-oil varied from 63.5–71.4 %.

CONCLUSIONS

In the present study, CFD modelling of four different biomass types in fluidized bed reactors was reported using an Eulerian-Eulerian CFD model combined with a comprehensive biomass reaction scheme. The result shows that cellulose-rich biomass produces more bio-oil than other biomass types. The yield of bio-oil produced by fast pyrolysis of oak was the highest, while the bio-oil yield produced by bagasse fast pyrolysis was the lowest. Moreover, the content of lignin has a close relationship with char production, and LIG-C is the main component of lignin to produce char. Furthermore, the contents of biomass components have a huge effect on the contents of bio-oil components, as they can influence the production and yields of products. The energy

recovery of bio-oil was also discussed in this paper. The ERCs of bio-oil obtained by fast pyrolysis of the four biomass types were in the range of 63.5–71.4 %.

NOMENCLATURE

Alphabetic Letters

A	pre-exponential factor (1/s)
C	heat capacity
c	coefficient
d	diameter (m)
E	activation energy (J/mol)
e	particle collision restitution coefficient
\bar{g}	gravitational acceleration (m/s ²)
h	specific enthalpy (J/kg)
H	heat-transfer coefficient (W/m · K)
HHV	high heating value (MJ/kg)
K	momentum exchange coefficient (kg/m · s)
k	heat conductivity (W/m · K)
\dot{m}	mass flow rate (kg/m ² · s)
p	pressure
q	heat transfer per surface area (W/m ²)
R	universal gas constant (W/m ²)
T	temperature (K)
v	velocity (m/s)
Y	mass fraction

Greek Letters

α	volume fraction
ρ	density (kg/m ³)
μ	viscosity (Pa · s)
τ	stress (Pa)
θ	granular temperature (m ² /s ²)

Table 8. Ultimate analysis and high heating values (HHV) of different biomass types and bio-oil obtained from pyrolysis of different biomass types, and bio-oil ERC

	Bagasse	Beech	Oak	Pine
C weight percentage (%) of biomass	49.22	49.13	47.88	49.35
H weight percentage (%) of biomass	6.00	5.93	5.98	6.02
O weight percentage (%) of biomass	44.78	44.94	46.14	44.63
O/C	0.910	0.915	0.964	0.904
HHV of biomass (MJ/kg)	19.46	19.38	19.05	19.52
C weight percentage (%) of bio-oil	45.55	46.40	46.36	46.93
H weight percentage (%) of bio-oil	6.52	6.49	6.52	6.62
O weight percentage (%) of bio-oil	47.93	47.12	47.12	46.44
O/C	1.052	1.016	1.016	0.990
HHV of bio-oil (MJ/kg)	18.63	18.97	19.00	19.39
Bio-oil ERC	63.5 %	67.9 %	71.4 %	68.7 %

γ collisional dissipation of energy
 φ energy exchange
 σ diffusion coefficient

Dimensionless Numbers

Re Reynolds number
 Pr Prandtl number
 Nu Nusselt number
 St Stokes number

Common Subscripts

g gas
 b biomass
 s sand
 i i^{th} gas species
 p sand or biomass
 D drag
 n gas or solid phase other than solid phase p

REFERENCES

- [1] E. V. Gonçalves, F. L. Seixas, L. R. de Souza Scandiuizzi Santana, M. H. N. O. Scaliante, M. L. Gimenes, *Can. J. Chem. Eng.* **2017**, 95, 1269.
- [2] A. V. Bridgwater, D. Meier, D. Radlein, *Org. Geochem.* **1999**, 30, 1479.
- [3] P. Mellin, Q. Zhang, E. Kantarelis, W. Yang, *Appl. Therm. Eng.* **2013**, 58, 344.
- [4] K. Papadikis, S. Gu, A. V. Bridgwater, *Chem. Eng. Sci.* **2009**, 64, 1036.
- [5] Q. Xue, T. J. Heindel, R. O. Fox, *Chem. Eng. Sci.* **2011**, 66, 2440.
- [6] Q. Xue, D. Dalluge, T. J. Heindel, R. O. Fox, R. C. Brown, *Fuel* **2012**, 97, 757.
- [7] P. Ranganathan, S. Gu, *Bioresource Technol.* **2016**, 213, 333.
- [8] H. Yang, R. Yan, H. Chen, D. H. Lee, C. Zheng, *Fuel* **2007**, 85, 1781.
- [9] J. Akhtar, N. S. Amin, *Renew. Sust. Energ. Rev.* **2012**, 16, 5101.
- [10] B. David, C. E. Douglas, *Can. J. Chem. Eng.* **1985**, 63, 94.
- [11] ANSYS Fluent Theory Guide, 15.0, ANSYS Inc., Canonsburg **2013**, <http://www.ansys.com/products/fluids/ansys-fluent>.
- [12] M. Patel, *Pyrolysis and gasification of biomass and acid hydrolysis residues*, PhD thesis, Aston University, Birmingham **2013**, p. 83.
- [13] J. Peng, Q. Eri, X. Zhao, *J. Renew. Sustain. Ener.* **2018**, 10, 013104.
- [14] D. Gidaspow, *Multiphase Flow and Fluidization*, 1st edition, Academic Press, San Diego **1994**.
- [15] D. J. Gunn, *Int. J. Heat Mass Tran.* **1978**, 21, 467.
- [16] F. Taghipour, N. Ellis, C. Wong, *Chem. Eng. Sci.* **2005**, 60, 6857.
- [17] F. Hernández-Jiménez, S. Sánchez-Delgado, A. Gómez-García, A. Acosta-Iborra, *Chem. Eng. Sci.* **2011**, 66, 3753.
- [18] C. K. K. Lun, S. B. Savage, D. J. Jeffrey, N. Chepur, *J. Fluid Mech.* **1984**, 140, 223.
- [19] M. Syamlal, *The Particle-Particle Drag Term in a Multiparticle Model of Fluidization*, Topical Report, National Technical Information Service, Springfield **1987**.
- [20] Q. Eri, X. Zhao, P. Ranganathan, S. Gu, *Fuel* **2017**, 197, 290.
- [21] E. Ranzi, M. Corbetta, F. Manenti, S. Pierucci, *Chem. Eng. Sci.* **2014**, 110, 2.
- [22] E. Ranzi, A. Cuoci, T. Faravelli, A. Frassoldati, G. Migliavacca, S. Pierucci, S. Sommariva, *Energ. Fuel.* **2008**, 22, 4292.
- [23] J. Blondeau, H. Jeanmart, *Biomass Bioenerg.* **2012**, 41, 107.
- [24] K. Papadikis, S. Gu, A. V. Bridgwater, *Energ. Fuel.* **2010**, 24, 2133.
- [25] J. Bruchmuller, B. G. M. van Wachem, S. Gu, K. H. Luo, R. C. Brown, *AIChE J.* **2012**, 58, 3030.
- [26] A. Anca-Couce, R. Mehrabian, R. Scharler, I. Obernberger, *Energ. Convers. Manage.* **2014**, 87, 687.
- [27] A. S. Kalgo, *The Development and Optimisation of a Fast Pyrolysis Process for Bio-oil Production*, PhD thesis, Aston University, Birmingham **2011**, p. 157.
- [28] M. G. Grønli, *A theoretical and experimental study of the thermal degradation of biomass*, PhD thesis, The Norwegian University of Science and Technology, Trondheim **1996**, p. 20.
- [29] B. E. Launder, D. B. Spalding, *Lectures in Mathematical Models of Turbulence*, Academic Press, London **1972**.
- [30] O. Authiera, B. Cluet, A. Delebarre, G. Mauviel, *Chem. Engineer. Trans.* **2014**, 37, 199.
- [31] D. K. Shen, S. Gu, K. H. Luo, S. R. Wang, M. X. Fang, *Bioresource Technol.* **2010**, 101, 6136.
- [32] T. N. Trinh, P. A. Jensen, K. Dam-Johansen, N. O. Knudsen, H. R. Sørensen, S. Hvilsted, *Energ. Fuel.* **2013**, 27, 1399.
- [33] E. Jakab, O. Faix, F. Till, *J. Anal. Appl. Pyrol.* **1997**, 40, 171.
- [34] C.-Y. Yin, *Fuel* **2011**, 90, 1128.
- [35] S. A. Channiwala, P. P. Parikh, *Fuel* **2002**, 81, 1051.

Manuscript received May 23, 2017; revised manuscript received December 5, 2017; accepted for publication December 5, 2017.